Multiple species laser-driven ion-shock acceleration

Brandon K Russell¹, Paul T Campbell¹, Alexander G R Thomas¹ and Louise Willingale¹

 1 Gérard Mourou Center for Ultrafast Optical Science, University of Michigan, Ann Arbor, Michigan 48109, USA

Abstract. Two-dimensional particle-in-cell simulations are used to explore laser-driven collisionless shock acceleration of ions in a multi-species plasma. Simple plasma slab simulations consisting of electrons, protons, and fully ionized carbon are used, varying the carbon ionization state, the relative fraction of ions, and the ratio of downstream to upstream plasma density. We find that two shocks can simultaneously propagate with different velocities defined by the dominant ion species reflected by each shock. The appearance of two shocks allows for ions to be accelerated twice, but can also cause trapping and heating of ions. We modify the current collisionless electrostatic shock theory where ions are treated as a single fluid to include a second ion fluid. This fluid model is unable to calculate the Mach number at which both ions will reflect, therefore we propose a kinetic model that may better model multi-species shocks. Scans are also performed in simulations with a laser pulse and realistic density profile that show reduced proton peak energies with the inclusion of carbon ions. Double shocks are only seen in simulations with steep density profiles, demonstrating the experimental importance of tailored density profiles.

1. Introduction

There is great interest in laser-driven ion acceleration for producing multi-MeV beams with small emittance and short temporal duration from plasmas. tuneable, quasi-monoenergetic and single species beam would be a desirable source for various applications across many scientific, technological and medical fields. A beam with these properties could be used in cancer therapy [1, 2], as an injector source for accelerators [3], as a picosecond resolution probe of large electromagnetic fields in high energy density physics experiments [4], as a compact and directional high energy neutron source [5, 6], to isochorically heat matter for warm dense matter experiments [7], and for isotope production for positron emission tomography [8]. Plasmas are a promising medium to provide a compact source because they can sustain huge electric fields, enabling acceleration to occur over very short distances.

Several laser-driven ion acceleration mechanisms have been identified and studied, each with unique properties that are highly dependent on both the target and laser pulse properties. The targets used are typically above the critical plasma density (overdense), $n_{crit} = m_e \varepsilon_0 \omega_L^2/e^2$, the density at which the plasma is opaque to a laser pulse of frequency ω_L . Strong transfer of laser energy to the plasma electrons occurs around n_{crit} . For relativistic intensities $(I_L \lambda_L^2 > 10^{18} \text{ Wcm}^{-2} \mu \text{m}^2)$, where the electrons oscillate in the laser fields to velocities approaching the speed of light, the modification of the effective mass of the electrons to $\langle \gamma \rangle m_e$, where $\langle \gamma \rangle$ is the time-averaged Lorentz factor, enables the propagation of the laser to the higher relativistic critical density $n_{\gamma crit} = \langle \gamma \rangle m_e \varepsilon_0 \omega_L^2/e^2$.

The most rigorously studied acceleration mechanism is target normal sheath acceleration (TNSA) [9]. It is a robust method for accelerating ions, using relatively thick foil targets (i.e. $n_e \gg n_{crit}$) to produce beams with excellent transverse emittance properties, making it suitable for imaging applications [10]. By reducing the target thickness to sub-wavelength thicknesses, it has been theorized that quasi-monoenergetic beams can be generated by radiation pressure acceleration (RPA) or light-sail acceleration, where the whole target is accelerated together [11]. Using such targets requires excellent laser contrast and very high-intensity laser pulses. Practically, small focal spot intensity gradients [12] or target instabilities [13] can limit RPA,

although there has been recent progress in mitigating these problems [14, 15].

A promising alternative mechanism that can generate narrow energy-spread spectral features is collisionless shock acceleration (CSA) [16, 17, 18, 19. An electrostatic shock is generated and used to reflect ions to high energies with a very small energy spread. Unlike RPA, this method does not require extreme laser pulse intensity contrast ratios, but instead requires tailored targets with density profiles that allow for the production of strong shocks while limiting the energy spread of the beam due to inherent TNSA by fields produced at the rear of the target [20]. Experiments by Haberberger et al. [17] and Palmer et al. [18] demonstrated that CSA can produce very narrow energy spread beams from the interaction of a laser with a marginally overdense hydrogen gas jet. The peak density and spatial profile of the target were found to be critical to the shock formation. In both cases CO₂ lasers were used due to their long emission wavelengths ($\lambda_L=10 \mu m$), reducing the target density needed to meet the critical density of the laser. In addition, Haberberger et al. used a train of pulses to generate a steep density gradient at the front edge of the target allowing for the production of a strong shock. This method accelerated proton beams with energies of ~ 20 MeV and extremely narrow energy spreads $\Delta E/E_{FWHM} < 1\%$.

Fiuza et al. subsequently derived the ideal conditions for laser-driven shock acceleration [21]. A set of 2D particle-in-cell (PIC) simulations showed that the conditions for producing a viable proton beam for proton therapy could be met with currently available lasers and realistic target density profiles. The ideal target density profile proposed in this report used a linear density ramp to a slightly overdense peak followed by an exponential density decay to suppress TNSA. The laser pulse incident on the linear ramp would isothermally heat the electrons to temperatures of ~MeV and cause density steepening near the peak, thereby generating the conditions for shock formation. A scan of accelerated proton energy as a function of normalized laser intensity a_0 showed that with this ideal profile, beams with energies >100 MeV could be produced with $a_0 \sim 10$.

Recent experiments have investigated several potential ways to produce this ideal density profile for laser systems producing pulses with a central wavelength of $\sim 1 \ \mu m$. At this wavelength n_{crit} is

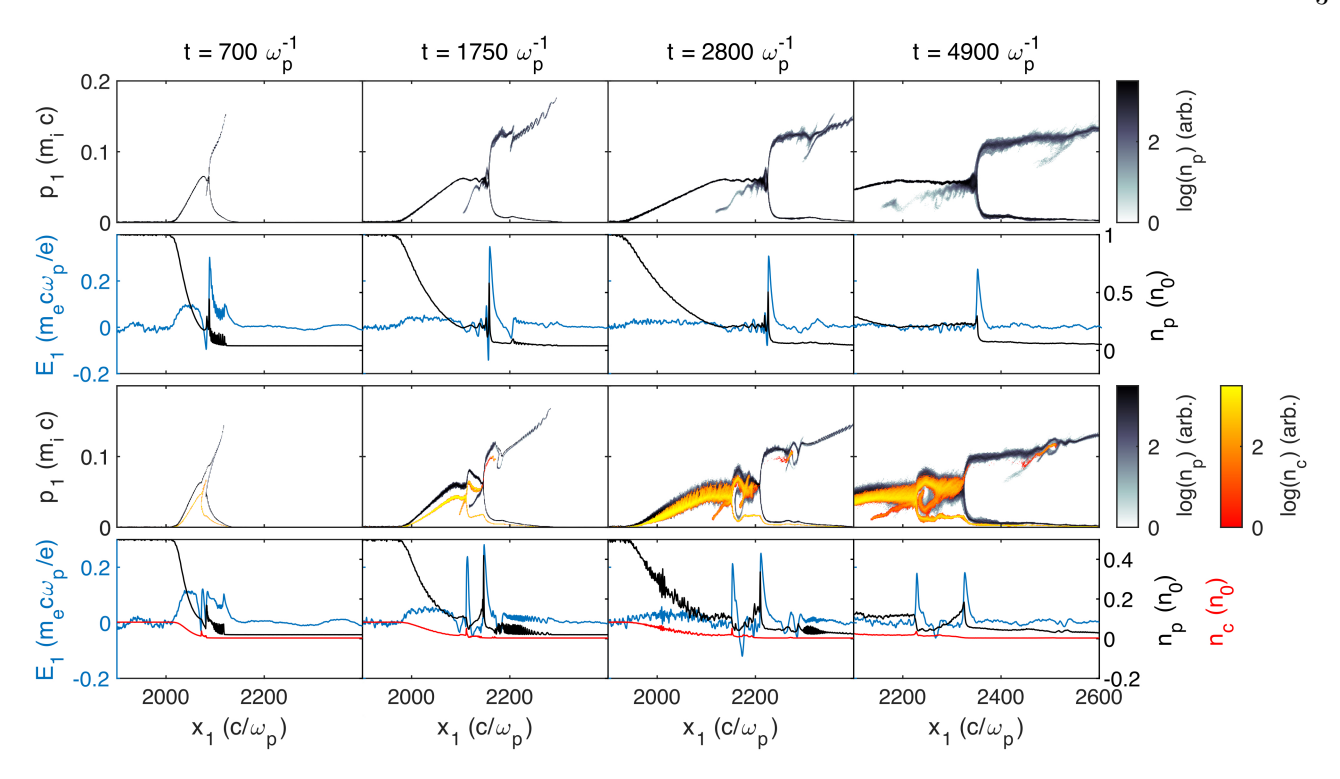


Figure 1. The propagation of shocks from plasma slab simulations for only protons (rows 1, 2) compared to $0.5n_e$ protons and C^{6+} (rows 3, 4). The ion phase space (rows 1, 3), and the electric field and ion densities (rows 2,4), are shown at different times as the shocks form and reflect protons or carbon ions.

at an intermediate density between a typical gas and a solid, making density profiles with sharp gradients and near-critical peak densities difficult to achieve. Pak et al. [22] used a 0.5 μ m thick Mylar target and a laser to ablate the back surface of the target to generate a rear scale length. Kordell et al. [23] used a cryogenically cooled supersonic Ar/H gas jet with a knife edge to modify the density profile of the gas jet. Hicks et al. [24] used a high pressure hydrogen gas jet to reach high densities, and additionally formed a blast wave using a lower power prepulse to produce a sharp density gradient on axis, similar to the work of Helle et al. [25]. Chen et al. used an extremely high pressure hydrogen gas jet [26], similar to that characterized by Sylla et al. [27]. These experiments were able to achieve overdense targets, but this was only achieved through the use of cooling, additional lasers, special high pressure valves and gas jets, or with a multi-species target due to the higher number of ionization states. This experimental reality is contrary to most shock theory where only a single ion species is considered. Although collisionless shock theory allows for multiple species by simply using an average ion mass and charge or by adding more terms to Poisson's equation when calculating the shock potential, these changes do not correctly incorporate the physics of an additional ion species.

Previous multiple ion species simulations have investigated intricacies that arise, such as instabilities in the upstream plasma due to the streaming of multiple species [28], in idealized low Mach number simulations below the critical Mach number [29], in specific cases to support experimental data [30], and at high laser intensities [31]. Shock formation in plasmas with multiple ion species has only been studied comprehensively for the collisional regime where collective effects drive the separation of ion species [32, 33].

To understand how the introduction of a heavy ion affects proton beam generation, here, we perform particle-in-cell (PIC) simulations consisting of three particle species (protons, electrons, C^{6+}). This three species scenario is relevant to the use of methane (CH₄) as a gas target or CH as a solid target for laser-driven shock acceleration. Section 2 reviews the current theory of single ion species shocks and what modifications are required to model multiple species shocks. Section 3.1 describes the simulations we have performed for multi-species shocks using the simple plasma slab model of Fiuza et al.. In section 3.2, we modify the laser-generated shocks demonstrated by Fiuza et al. to investigate whether the properties seen in the idealized plasma slab simulations are also observed in the more realistic simulations of laser-plasma interactions. At the end of section 3.2 we discuss our findings and what implications these simulations have for future experiments.

2. Collisionless Electrostatic Shock Theory

Collisionless shock acceleration has been theorized for the last 50 years or so, with much of the theory being first derived by Sagdeev [34]. In Sagdeev's theory, basic conservation and electrostatic equations were used to describe the conditions for the formation of a soliton and for this soliton to reflect ions and become a shock. Conservation of mass and energy were used to describe the relation between the velocity and density of ions in some potential ϕ . Electrons were assumed to follow a Boltzmann distribution, $n_e(\phi) = n_{e0}e^{e\phi/k_BT_e}$, and charge neutrality was assumed. These densities were used in Poisson's equation

$$\nabla^2 \phi = \frac{e(n_{e0}e^{e\phi/k_B T_e} - Zn_i(\phi))}{\epsilon_0}.$$
 (1)

All terms in this equation are functions of ϕ , allowing us to take an integral with respect to ϕ to form

$$\frac{1}{2}(\nabla\phi)^2 + \Psi(\phi) = 0. \tag{2}$$

Using the condition that $\nabla \phi = 0$ when $\phi = 0$ to solve for the constant of integration gives the equation for a soliton. Here $\Psi(\phi)$ is the nonlinear Sagdeev potential given by

$$\Psi(\phi) = P_i(M, \phi) - P_e(\phi), \tag{3}$$

where P_i and P_e are the particle pressures and M is the Mach number given by the ratio of the shock velocity u to the upstream sound speed $C_s = \sqrt{Zk_BT_e/m_i}$. We can note that if this soliton has a peak potential ϕ_{max} greater than the kinetic energy of the ions it interacts with, these ions cannot pass the soliton and will reflect to form a shock. This reflection condition is given as

$$Ze\phi_{max} > m_i u^2/2. (4)$$

By noting that $\nabla \phi = 0$ when $\phi = \phi_{max}$, we can substitute the reflection condition into equation 2 and solve numerically for ϕ_{max} . As was found by Sagdeev, $e\phi_{max} \approx 1.3k_BT_e$, and therefore by substituting back into the reflection condition

$$M_{cr} = \frac{u}{\sqrt{Zk_BT_e/m_i}} \approx 1.6,\tag{5}$$

where M_{cr} is the critical Mach number.

Since the initial derivation by Sagdeev, this method for deriving the conditions for reflection has been used for many situations, sometimes with slight modifications. Sorasio *et al.* treated the electrons kinetically, assigning separate densities to the electrons ahead of the shock (upstream) and behind the shock (downstream) [35]. These modifications allowed for $M_{cr} > 1.6$ when the electron temperature and density are not the same in the shock upstream and

downstream. The ratio of downstream to upstream electron density was given by $\Gamma = n_{e,down}/n_{e,up}$ and the temperature ratio was given by $\Theta = T_{e,down}/T_{e,up}$. This theory was later generalized by Stockem *et al.* to include relativistic effects, allowing for relativistic electron temperatures, relevant to high-intensity laser driven shocks to be considered here [36].

These theories treat the ions as a single fluid, which is integral to finding the reflection condition. As will be shown here, a single fluid treatment of the ions cannot correctly predict the structure of multispecies shocks. The standard ion density equation can be derived using conservation of mass, $n_i u = n_{i0} u_0$, and conservation of energy, $m_i u^2/2 = m_i u_0^2/2 - Ze\phi$. Combining these equations gives

$$n_i(u_0, \phi) = \frac{n_{i0}}{\sqrt{1 - \frac{2Ze\phi}{m_i u_0^2}}}.$$
 (6)

We can then substitute into equation 1 and normalize the potential $\hat{\phi} = e\phi/k_BT_e$ and spatial dimensions $\chi = x/\lambda_D$ where $\lambda_D = \sqrt{\epsilon_0k_BT_e/e^2n_{e0}}$ is the Debye length. Solving for the Sagdeev potential of a soliton will then give the ion pressure

$$P_i(M, \hat{\phi}) = M^2 \left(1 - \sqrt{1 - 2\hat{\phi}/M^2} \right).$$
 (7)

If we now consider a multi-species plasma with two ions that make up a fraction α and $1-\alpha$ of the ion number density respectively, the Sagdeev potential will include two terms for ion pressure with different Mach numbers,

$$P_{i,l}(M_l, \hat{\phi}) = \hat{Z}_l \alpha M_l^2 \left(1 - \sqrt{1 - 2\hat{\phi}/M_l^2} \right),$$
 (8)

$$P_{i,h}(M_h, \hat{\phi}) = \hat{Z}_h(1-\alpha)M_h^2 \left(1 - \sqrt{1 - 2\hat{\phi}/M_h^2}\right), (9)$$

where $\hat{Z}_i = Z_i/(\alpha Z_l + (1-\alpha)Z_h)$, and h and l represent the heavy and light ion respectively. If we follow the standard shock analysis and input the potential to reflect one of the ions, i.e. $\hat{\phi}_{max} = M_l^2/2 = u_{i,l}^2/(2Z_lk_BT_e/m_{i,l})$, then $P_{i,l} = \hat{Z}_l\alpha M_l^2$. Therefore, we can note that ion reflection corresponds to the argument of the square root going to zero, and for larger potentials the ion pressure becomes imaginary as our assumption that the ion distribution is that of a single fluid and can be described by equation 6 becomes invalid. If we assume that the two ion species have the same upstream fluid velocities, then the ratio of Mach numbers $M_l/M_h = \sqrt{Z_h m_{i,l}/Z_l m_{i,h}}$. Following the analysis to obtain M_{cr} for each ion, one finds that it is imaginary for the heavy ion and therefore can only be solved for the higher charge to mass ratio (light) ion. This is because our fluid assumption for the light species will break down for $\hat{\phi} > M_l^2/2$, i.e. equation 8 becomes imaginary, however reflection of the heavy species is expected to occur when $\hat{\phi} > M_h^2/2$. $M_h > M_l$, therefore the light ion pressure will be imaginary in the range of Mach numbers where the heavy ion critial Mach number is expected to occur, invalidating the calculation of M_{cr} for this ion.

Once reflections occur, energy will be transferred from the shock to the reflected ions, thereby slowing the shock. This limits the shock velocity to be approximately given by M_{cr} . From our previous analysis we may then expect that a shock propagating through a multi-species plasma will be limited by the Mach number necessary to reflect the light ion species, therefore heavy ions will remain as a fluid background. Our simulations show this is only partially true. As expected, most of the light ions will reflect, but this leaves the shock downstream dominated by the heavy ion species. This allows for the formation of a second, slower shock that reflects the heavy ions and also interacts with the light ions that do not meet the reflection condition of the primary shock. The dynamics of this double shock will be explored in the following sections.

3. Simulations

3.1. Plasma Slab Shock Model

In the work by Fiuza et al. a simple simulation model of two semi-infinite plasma slabs was used to study shock formation based on the initial temperature ratio Θ and density ratio Γ between the slabs [21]. directly build from this work, we used the same model, only modifying the ion species used. This simulation model is useful for elucidating the underlying physics because it removes the complexities of the laser-plasma interaction and a realistic density profile. Simulations were performed using the 2-dimensional OSIRIS 4.0 PIC code [37, 38]. A simulation box with dimensions $4098 \times 128(c/\omega_n)^2$ with a grid of 8196×256 cells was used. Periodic boundary conditions in the x_2 direction, perpendicular to the shock propagation, create effectively infinite plasma slabs. The simulations ran for $5000\omega_p^{-1}$ with a time step of $0.35\omega_p^{-1}$. Two ion species were used, one with the equivalent charge-tomass ratio of a proton, and another equivalent to fully ionized carbon. Each particle species was initialized with 36 particles per cell. The x_1 direction was divided evenly into two plasma slabs with different densities consisting of cold ions, and electrons with a uniform temperature of 1.5 MeV ($\Theta = 1$) represented by a Maxwell-Jüttner distribution. A simulation box much larger in the shock propagation direction than the distance travelled by the reflected ions during the duration of the simulation was used to reduce

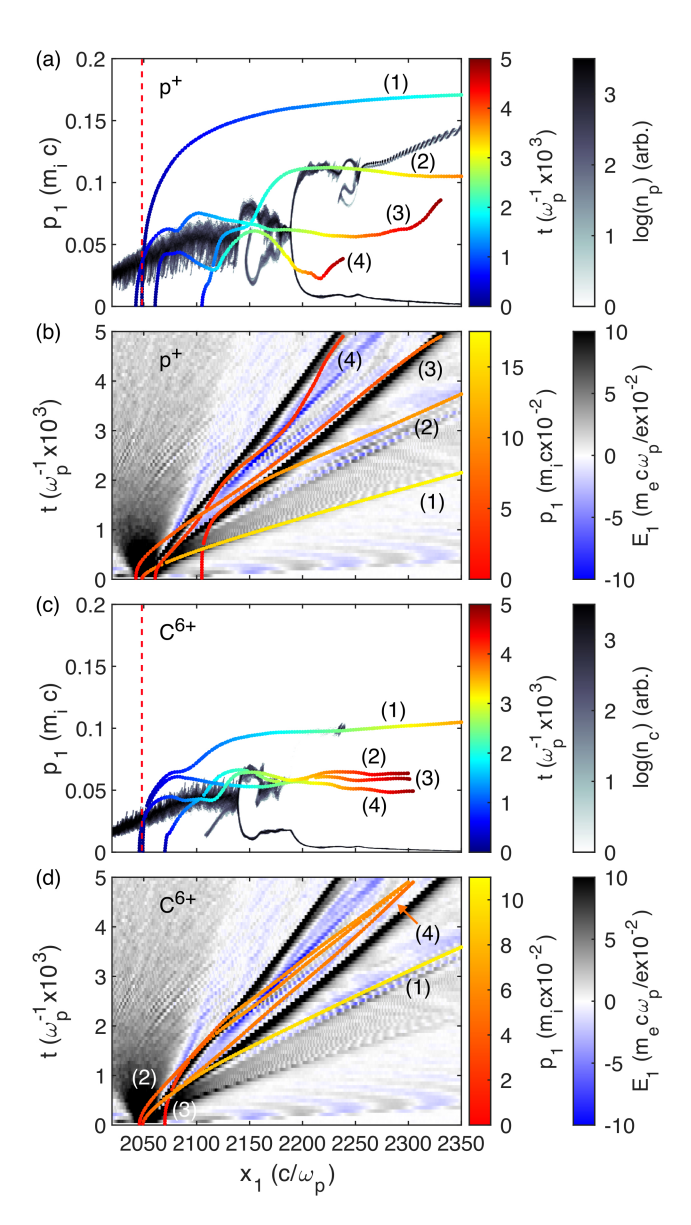


Figure 2. Selected characteristic trajectories of (a-b) protons and (c-d) C^{6+} overlaid on their respective phase space profiles at $t=2450\omega_p^{-1}$ and temporal maps of E_1 where the dotted red line denotes the initial interface between the slabs with an initial density ratio $\Gamma=25$.

acceleration due to TNSA and boundary-effects.

Figure 1 shows the characteristic propagation of a multi-species shock (with an equal charge density contribution by protons and carbon ions) compared to that of a single species proton shock where the initial plasma density ratio between the downstream $(x_1 < 2048c/\omega_p)$ and upstream slabs $(x_1 > 2048c/\omega_p)$ $\Gamma = 25$, i.e. the single species case closely replicates the result presented in reference [21]. The $\Gamma = 25$ data is reported here because significant ion reflection occurs at this density ratio. As will be shown later, at smaller values of Γ the shocks become weak and

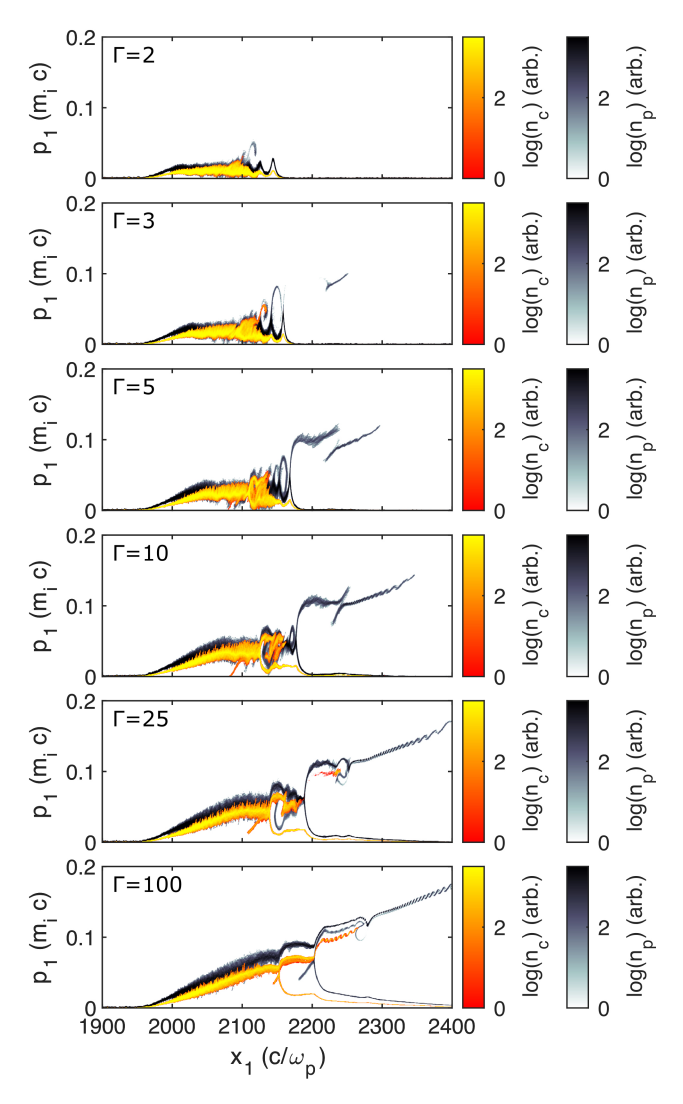


Figure 3. Plasma slab proton and ion momentum evolution at $t=2450\omega_p^{-1}$ using various Γ with an initial $T_e=1.5$ MeV and $n_p=0.5n_e$.

reflections are negligible. In both the single and multispecies cases, shocks were formed from an ion acoustic wave driven by instabilities due to the propagation of the more dense electrons of the downstream slab into the less dense upstream slab. As the electrons propagate into upstream, they generate a space-charge field that pulls the ions at the edge of the slab toward the upstream direction, this is seen in the decaying boundary between the slabs. Ions in the shock upstream that meet the reflection condition are reflected, steepening the electrostatic field. Ions that do not meet the reflection condition propagate through the shock into the downstream where they are decelerated in the frame of the shock.

In the multi-species case two shocks are formed, a feature that has not been previously observed in

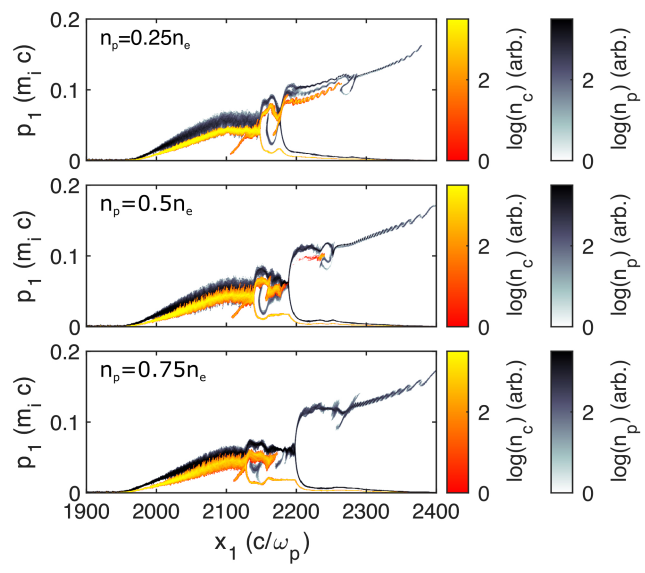


Figure 4. Plasma slab proton and ion momentum evolution at $t=2450~\omega_{\rm p}^{-1}$ using a $\Gamma=25$ with an initial $T_e=1.5~{\rm MeV}$ and n_p is varied as shown in the plot.

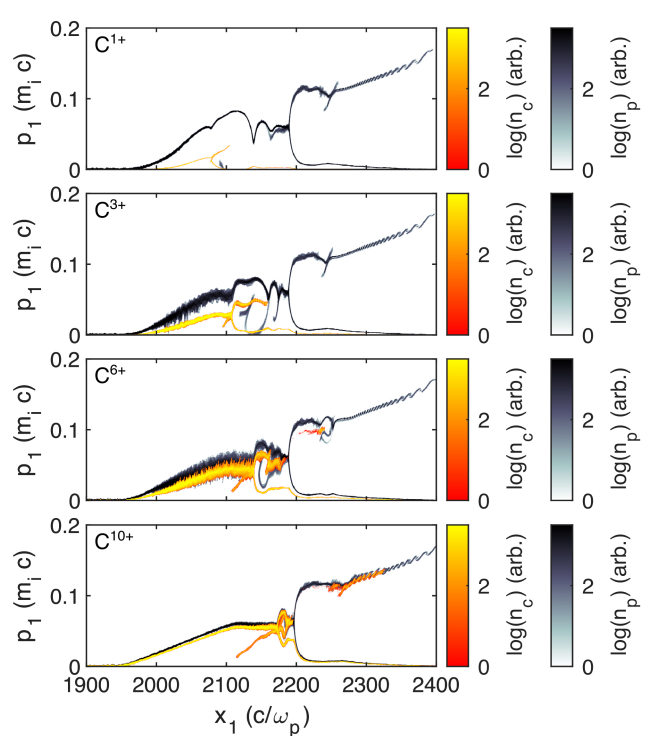


Figure 5. Plasma slab proton and ion momentum evolution at $t=2450~\omega_{\rm p}^{-1}$ using a $\Gamma=25$ with an initial $T_e=1.5$ MeV and the ionization state of the carbon ion is varied while the charge density is held constant. Note the fictional C^{10+} ionization state is included to observe the trend.

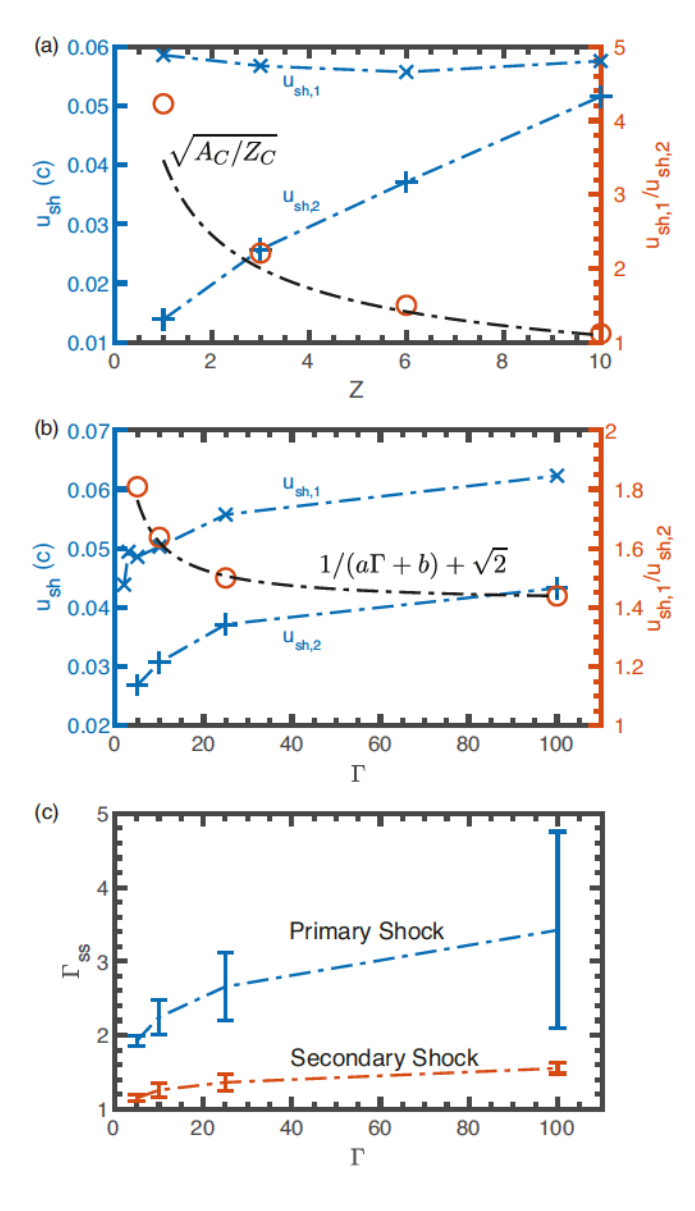


Figure 6. Velocities in the lab-frame of the primary (reflects p⁺) and secondary (reflects C^{Z+}) shocks generated from semi-infinite slabs with a uniform electron temperature of 1.5 MeV and various (a) charge-to-mass ratios from figure 5 and (b) density ratios Γ from figure 3. The ratio of velocities as a function of Γ is approximately given by $1/(a\Gamma + b) + \sqrt{2}$ where $a \approx 0.4$ and $b \approx 0.88$. The steady-state ratio of electron densities across the shocks Γ_{ss} differs from the initial ratio Γ shown in (c) at $t = 2450 \ \omega_{\rm p}^{-1}$.

single species and low-Mach number multi-species simulations, but was recently reported at high laser intensities [30, 31]. From the theory shown in section 2, we would expect a single shock to form that only reflects protons, the higher charge-to-mass ion species. One reason this is not true is due to the change in the downstream plasma conditions of the primary shock which are effectively the upstream conditions of the secondary shock. During the formation time of the shocks, the primary shock meets the reflection condition for the protons first which slows the shock, limiting the maximum speed to be close to that given by M_{cr} . Due to the protons being initially cold, if the shock condition is met then almost all the protons will reflect. We calculated the Mach number of the primary shock from the simulations using the average upstream Z and atomic number A which were approximately 1.7 and 2.5 respectively. The velocity of the primary shock was $\sim 0.056c$ corresponding to a Mach number of ~ 1.7 . Due to the larger shock potential required to reflect the carbon ions, they are only accelerated in the positive x_1 direction by the electrostatic field of the primary shock to a velocity smaller than both the primary and secondary shocks, allowing the ions to propagate into the primary shock downstream and subsequently interact with the secondary shock. This forms an upstream for the secondary shock made primarily of carbon ions that have been accelerated in the laboratory frame, corresponding to a deceleration in the frame of the secondary shock, allowing them to meet the reflection condition at lower potentials. To calculate the Mach number of the shock we used the average upstream Z and A only including those ions with velocities smaller than the secondary shock velocity, i.e. the ions that interact with the shock. This resulted in $A \approx 8.1$ and $Z \approx 4.2$, with a shock velocity of $\sim 0.037c$ this corresponds to a Mach number of ~ 1.3 . If we consider the upstream carbon ion velocity $(\sim 0.016c)$ in this calculation by subtracting it from the shock velocity then this only gives a Mach number of ~ 0.7 .

To better understand the reflections from the double shock, particle tracking was performed. Using the multi-species simulation shown in figure 1, particles were randomly chosen from both the carbon and proton populations with $p_1 > 0.05 m_i c$ and $x_1 > 2142 c/\omega_p$ at $t = 2450 \omega_p^{-1}$. Many of these particles followed very similar phase space trajectories, however a few characteristic phase space trajectories were identified and have been plotted in figure 2. Four general trajectories were found for the protons and are overlaid on the proton phase space and electric field in figure 2(a-b). Tracks (1) and (2) represent reflected protons that originated from the edge of the dense slab $(x_1 = 2048 c/\omega_p)$ and from the low density

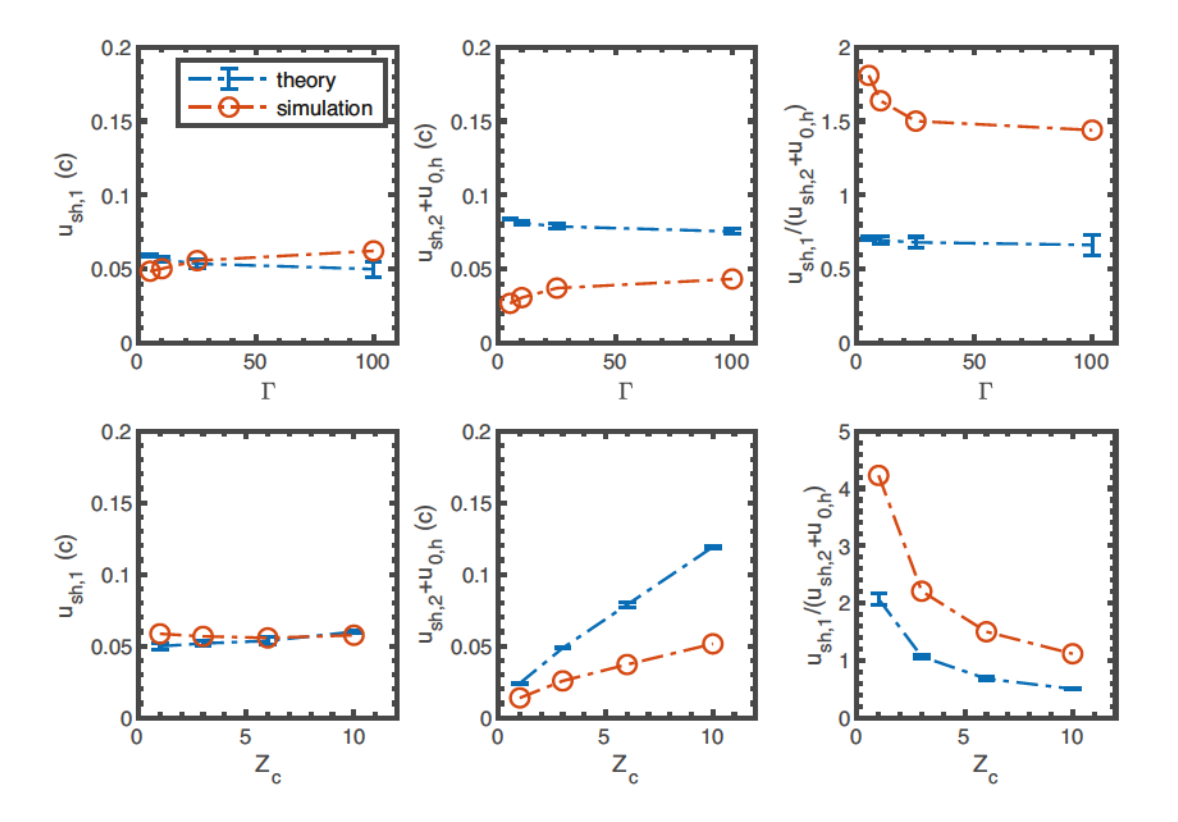


Figure 7. Comparison of simulated shock velocities with those calculated from equations 12 and 15 using Γ_{ss} from the simulations. The top row is for varying Γ and the bottom row is for varying Z_c .

slab respectively. Track (1) represents the highest energy protons that are transiently reflected during shock formation and can be seen in figure 1 as the cause of the break in the reflected ions in phase space. Macchi et al. [39] also noted this break in laserdriven shock simulations, and found that it was caused by oscillations of the electrostatic component of the shock at early times. Track (2) is representative of the steady-state reflection of the low density slab protons being reflected by the shock. Track (3) represents the trajectory of protons that originate further into the high density slab. From figure 2(b) this particle experiences smaller initial electric fields than that of track (1) resulting in a smaller initial velocity given by the inverse slope of the track. This velocity is larger than the steady-state velocity of both shocks. allowing the particle to move from the secondary shock downstream into the primary shock downstream and begin to be accelerated by the primary shock at late times. Finally, track (4) represents protons from the low density slab that did not meet the shock condition, and instead pass through the shock. These protons become trapped between the two shocks, generating a spiral in phase space.

Very similar trajectories are seen for the carbon ions in figure 2(c-d). The exception is for track

(1), that shows two stages of acceleration where it is reflected by the trailing secondary shock and then further accelerated by the primary shock. This only occurs very early in the shock formation when carbon ions reflected from the secondary shock can propagate just ahead of the primary shock to gain energy from the electrostatic fields. It should be noted that the secondary acceleration the carbon ion experiences at the primary shock is not a reflection. At intermediate times, in figure 1 we can see that carbon ions reflected from the secondary shock are accelerated to velocities too small to pass through the primary shock and are instead decelerated by the oscillatory fields and trapped between the shocks. These oscillatory fields are observed between the shocks in figure 2(d), increasing the slope of the ion trajectories, corresponding to deceleration of the ions. At late times, when the primary shock slows and the electrostatic fields weaken, we can see that some carbon ions begin to pass the primary shock.

To further study the characteristics of these multispecies shocks, we varied the ratio of densities Γ , the ratio of protons to carbon ions, and the charge-to-mass ratio of the carbon ions. The results of the simulations scanning Γ are shown in figure 3. A similar study by Fiuza *et al.* for a purely proton shock found that

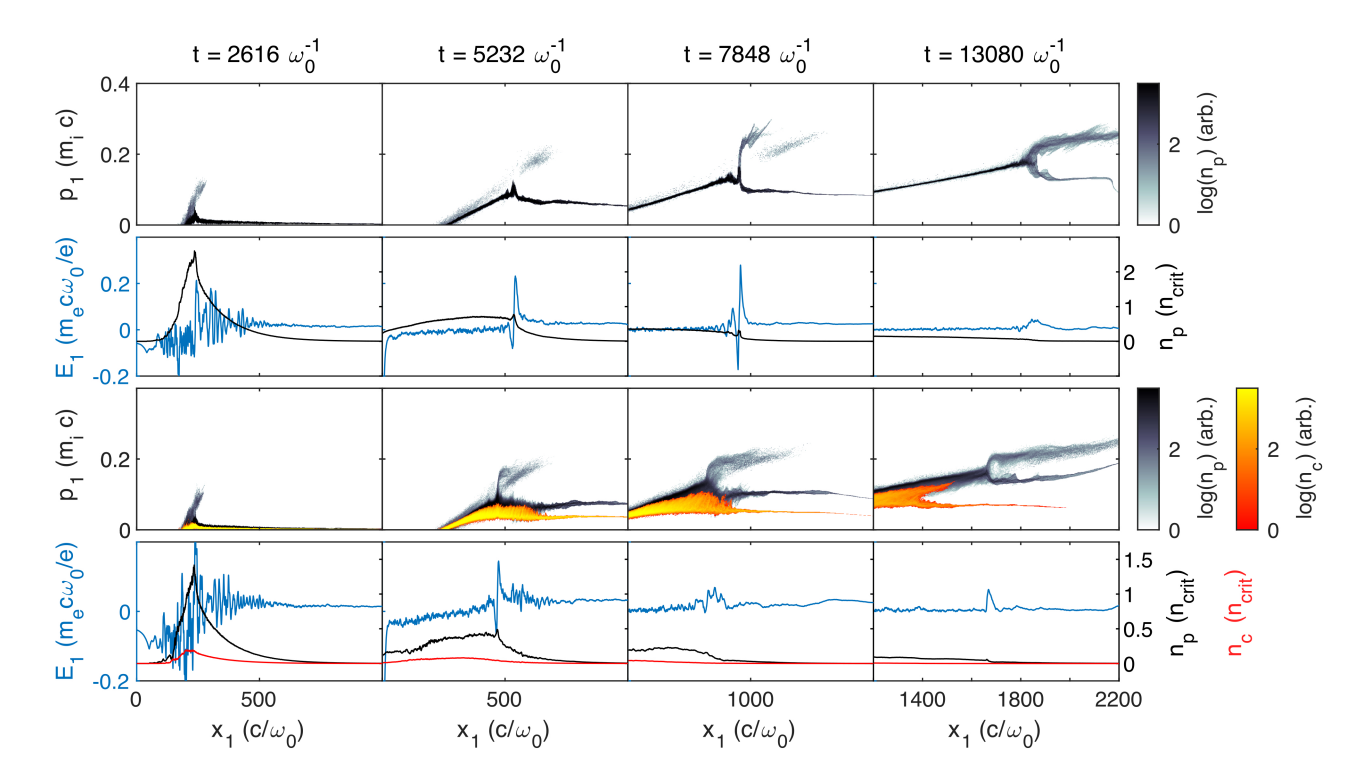


Figure 8. Propagation of a laser-driven single ion species shock (rows 1 and 2) and multi-species plasma shock (rows 3 and 4). The proton and ion phase space (rows 1, 3), and the electric field and proton and ion densities (rows 2,4), are shown at different times as the shocks form and reflect protons or ions.

for $\Gamma \approx 2$ an ion acoustic wave is driven as the high density slab expands into the low density slab, but ion reflection does not occur until larger density ratios of $\Gamma > 4$ [21]. When the charge density consists of equal parts protons and C^{6+} , we observe slightly different results. In the case of $\Gamma = 2$, protons are accelerated and trapped due to the buildup of carbon ions. By $\Gamma =$ 3, the acceleration and trapping of C^{6+} begins a few oscillations behind the leading edge of the ion acoustic wave and protons are seen to reflect. For increasing Γ , the Mach number of both the primary and secondary shocks are increased, enabling significant ion reflection. When $\Gamma = 100$, the C⁶⁺ trapping becomes low enough such that these ions can interact with the primary shock, allowing them to be boosted to even higher energies. This results in three co-propagating bunches of ions with slightly different energies. For the carbon ions to meet this boosting condition the velocity of the reflected ions must exceed the shock velocity of the primary shock. The boosted protons are not reflected, instead seeing a double boost as they move from the secondary shock downstream into the primary shock upstream. In figure 4 it can be seen that by reducing the number of protons and increasing the number of carbon ions to maintain the initial neutrality, the necessary Γ to meet the boosting condition is reduced. This is due to the secondary shock velocity increasing,

while the primary shock velocity decreases.

The effect on the shock structure by varying the ionization state of carbon (i.e. the charge-to-mass ratio) is shown in figure 5. Plotting the measured velocities for the measured parameter space (figure 6(a)), it is found in the high-Mach number limit (large Γ), the ratio of shock velocities approximately scales as $\sqrt{A_C/Z_C}$ where A_C is the atomic number of carbon and Z_C is the ionization state. The scan includes the fictional ionization state of C^{10+} to extend the trend. Plotting the velocity of the shocks as a function of Γ for C^{6+} (figure 6(b)) and fitting to the ratio of the primary to secondary shock velocities gives $u_{sh,1}/u_{sh,2} \propto 1/(a\Gamma+b) + \sqrt{2}$ where $a \approx 0.4$ and $b \approx 0.88$. We can also note from figure 4 that changing the fraction of ion species will also change the ratio of shock velocities.

In deciding how to model these trends we made a few important considerations. Firstly, the initial conditions outlined in the simulations e.g. density ratios Γ and ion fluid velocities evolve to a set of steady-state conditions which can be greatly different from the initial conditions. This is a problem because the current models define the shock properties at steady-state, therefore we would need to also model the evolution of these properties. Although Γ is defined for the electrons, from figure 1 rows 2 and 4 we can

see how the density ratio decays for the ions from an initially large ratio to a much smaller ratio at the shock steady-state. This steady-state ratio Γ_{ss} is shown for the primary and secondary shocks in figure 6(c)which shows that although the density ratios start at very different values, they decay to very similar ratios. Secondly, ion fluid velocities in the shock upstreams differ from the initial values due to acceleration by electric fields formed by reflected ions and for the secondary shock upstream, acceleration by the primary shock. The acceleration by the primary shock can greatly affect the fluid velocity of the ions in the secondary shock upstream as demonstrated by figure 5. Thirdly, the double shock structure is made of many populations of ions e.g. reflected and trapped which require a kinetic description. Finally, we must note that although we are simply changing the charge of the carbon ions in figure 5, the number density of these ions will also change to maintain the charge density.

Although a rigorous model will need to treat the ions kinetically as we will later discuss, as a first attempt we made approximations to model the ions as two fluids and the shocks as being independent. For the purpose of our simple model we assumed that the primary shock was made of two ion species, reflecting only the light ion species, and the secondary shock was a single species shock only including the heavy ion species. The primary shock was modeled using the relativistic electron pressures derived by Stockem *et al.* [36],

$$P_{e,up}^{r}(\hat{\phi}, \Gamma_{ss}) = \frac{\hat{\phi}(1-\mu_0)}{1+\Gamma_{ss}},$$
 (10)

$$\begin{split} P^{r}_{e,down}(\hat{\phi},\Gamma_{ss},\Theta) &= \\ \frac{\hat{\phi}\Gamma_{ss}}{\Theta(1+\Gamma_{ss})} \left[\hat{\phi} \left(1 - \frac{\mu_{0}}{\Theta} \right) + \Theta \left(1 + \frac{\mu_{0}}{\Theta} \right) \right], \quad (11) \end{split}$$

where $P_{e,up}$ and $P_{e,down}$ are the upstream and downstream electron pressures in the relativistic limit where $\mu_0 = m_e c^2/k_B T_e \ll 1$ is the normalized upstream electron temperature, and Θ is the ratio of downstream to upstream electron temperatures. The Sagdeev potential can then be constructed from these electron pressures and the multi-species ion pressures we derived in equations 8 and 9. To solve for the Mach number to reflect the light ion species we set $\hat{\phi} = M_l^2/2$ and $\nabla \phi = 0$ in equation 2. Solving for M_l gives the critical Mach number $M_{cr,l}$,

$$M_{cr,l} = \sqrt{2\Theta \left[\frac{2\zeta - 1 + \mu_0}{\Gamma_{ss}(1 - \mu_0/\Theta)} + \frac{2\zeta - 1 - \mu_0/\Theta}{1 - \mu_0/\Theta} \right]}, \quad (12)$$

$$\zeta = \hat{Z}_l \alpha + \frac{Z_l A_h}{Z_h A_l} \hat{Z}_h (1 - \alpha) \left(1 - \sqrt{1 - \frac{Z_h A_l}{Z_l A_h}} \right). \tag{13}$$

In the case of a single species ($\alpha = 1, \zeta = 1$) these equations simplify to equation 12 in the report by Stockem et al. [36]. We used this single species equation to calculate the velocity of the secondary shock assuming a heavy ion only plasma. obtain the ratio of the primary shock velocity to the secondary shock velocity we assume that the shocks will move at the velocity needed to reflect the light and heavy ions respectively at steady state $u_{sh,1} = \sqrt{Z_l k_B T_e / m_{i,l}} M_{cr,l}$ and $u_{sh,2} =$ $\sqrt{Z_h k_B T_e/m_{i,h}} M_{cr,h}$. We must also take into account the fluid velocity of the heavy ions in the upstream of the secondary shock because M_{cr} is calculated in the frame where the upstream ions are stationary. Using conservation of energy and noting that $\hat{\phi} = M_l^2/2$ gives the velocity of the heavy ions in the laboratory frame as,

$$u_{0,h} = u_{sh,1} \left[1 - \sqrt{1 - \frac{Z_h A_l}{Z_l A_h}} \right].$$
 (14)

This velocity is due to the acceleration of the heavy ions as they pass through the electrostatic fields of the primary shock without being reflected. We can then calculate the ratio of shock velocities as:

$$\frac{u_{sh,1}}{u_{sh,2} + u_{0,h}} = \frac{1}{1 + u_{sh,2}/u_{sh,1} - \sqrt{1 - Z_h A_l/Z_l A_h}}.$$
 (15)

To plot these equations we used Γ_{ss} calculated from the average of electron densities on either side of both shocks as shown in figure 6(c). This value varies for changes in both the initial Γ and the choice of carbon charge state Z. The ratio of electron temperatures across the shocks Θ can differ from unity and can be different for both shocks, but we found the temperature to be similar to the initial isothermal conditions in this case. Figure 7 shows the values calculated from equation 12 for the primary and secondary shock velocities compared to the values extracted from the simulations. For changing Γ and Z, the theory predicts similar values to the simulations for $u_{sh,1}$, although the trends are not correctly modeled. This discrepancy may be due to many of the properties not captured by the model e.g. reflections, upstream ion drift velocity, etc. which could have a small effect on the shock velocity. The theory overestimates the secondary shock velocity by a factor of 2-3 in both the Γ and Z scans, although it predicts a similar trend for the Z scan. The simulations show that the secondary shock velocity should be closer to the primary shock velocity, suggesting that protons cannot be neglected in the secondary shock.

In a rigorous model of the secondary shock, the protons should be included in two populations:

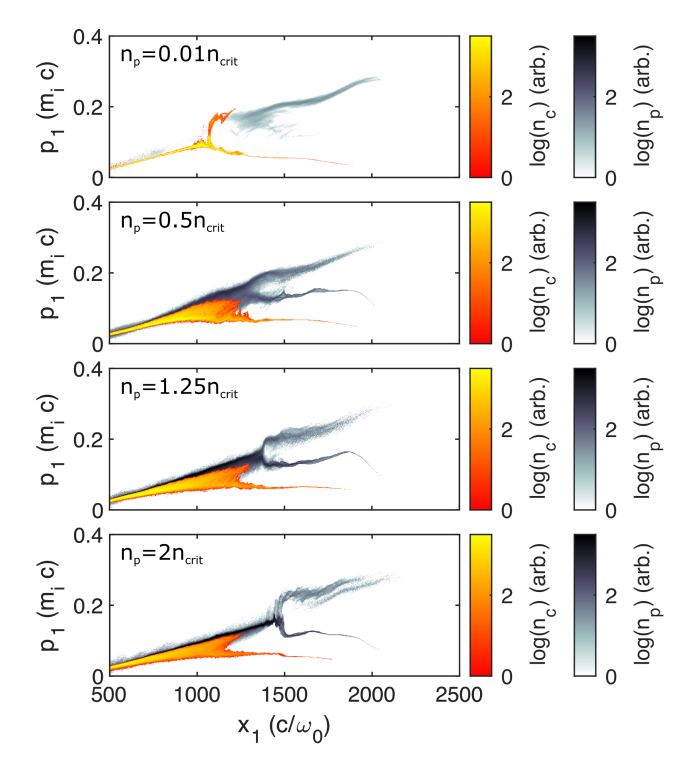


Figure 9. Comparison of multi-species laser driven shocks using the ideal density profile and a cumulative ion charge density of $2.5n_{crit}$ at $t=11366c/\omega_0$.

protons that freely drift from the shock downstream to upstream, and trapped protons in the shock upstream. This kinetic treatment could build from the model for a single species including reflections proposed by Malkov et al. [40]. In this kinetic model one also needs to consider the electron distributions on either side of the shock. In the model of Stockem et al. used here, the downstream of both shocks is assumed to be made of two population of electrons: trapped and free. The trapped electrons are assumed to follow the maximum density trapping approximation [41]. This approximation may not be true between the shocks. In our simple analysis the shocks were taken to be independent, therefore the upstream electron distribution of the secondary shock was taken to be a Maxwell-Jüttner distribution. These shock are coupled, therefore the upstream distribution of the secondary shock should match that of the primary shock downstream. A kinetic model would be very useful in accurately estimating reflected ion energies which cannot be done with the simple model presented here.

3.2. Laser-Driven Shock

In order to connect the conclusions from the slab simulations to laboratory experiments, we explored

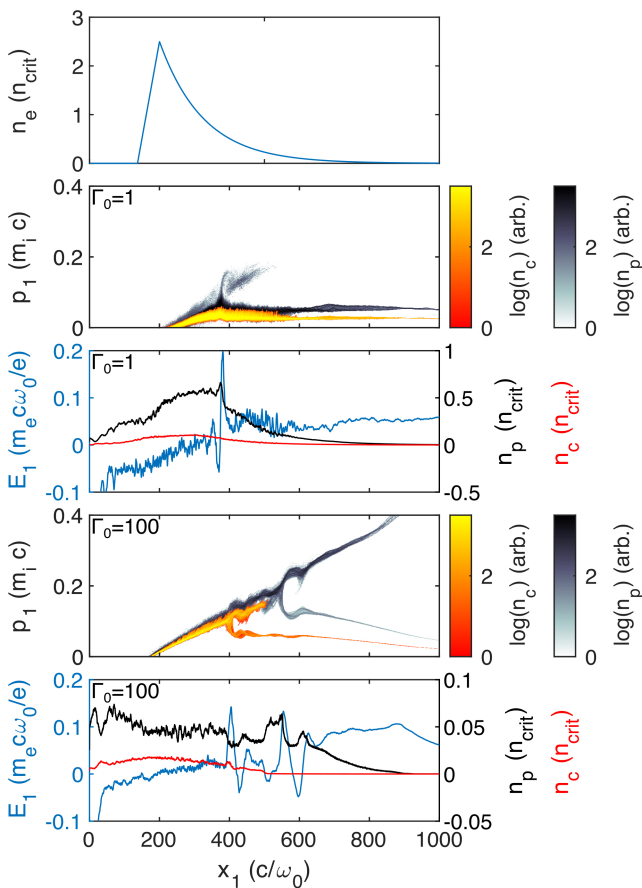


Figure 10. Comparison of laser driven shocks at $t = 4360c/\omega_0$ using a modification of the initial ideal density profile shown in row 1 where Γ_0 is the initial ratio between the peaks of the density up-ramp and decay.

laser-driven shocks by adapting the ideal profile described by Fiuza et al. to include multiple ion species. These simulations were performed in 2D with a $3840 \times 240 (c/\omega_0)^2$ simulation box and a grid of 12288×768 cells. A laser pulse with infinite spot size and a normalized intensity $a_0 = 2.5$ was injected to propagate along the x_1 -direction of the simulation box, linearly polarized in the x_2 -direction. The rise and fall time of the laser pulse was $2473.9\omega_0^{-1}$, equivalent to a 1 ps full-width half-max pulse duration for a 1 μ m wavelength laser. The laser was incident on a density profile consisting of $2.5n_{crit}$ electrons and a combination of protons and C^{6+} with a cumulative charge density equal to that of the electrons. Each species was initialized with 36 particles per cell. The density profile used a linear increase over $10\lambda_0$ followed by an exponential decrease with a characteristic decay length of $20\lambda_0$ where λ_0 is the wavelength of the laser [21].

Just as in the case of the plasma slab, we compared the single species shock formation with that of the multi-species shocks as shown in figure 8. The laser pulse incident on the rising edge of the density profile accelerates electrons into the plasma, generating a return current that also acts to heat, creating a uniform electron temperature. The overdense target and a high-intensity laser pulse allow for density steepening to occur near the peak of the profile and a shock to form. In both cases, a single shock is formed near the density peak that propagates, only reflecting protons. Electron heating in the single-species and multi-species simulations was compared by looking at the electron phase space (p1 vs. x1). The phase spaces were very similar at all times, giving comparable electron temperatures of $\sim 0.9 \text{ MeV}$ at $t = 7848\omega_0^{-1}$ in the shock upstreams of the single and multi-species simulations, suggesting that heating is similar in both cases. We performed several simulations with different ion ratio compositions, but in all cases only a single shock was formed (figure 9). This is inconsistent with the results found with the semi-infinite plasma slabs. Although at late times the multi-species phase space appears to show reflected carbon ions, the acceleration of these carbon ions occurred in the shock upstream due to streaming instabilities [28], and near the shock as the ions cross the electrostatic potential without being reflected. A notable result was found at extremely low fractions of protons $(0.01n_{crit})$ where protons are initially reflected, and later, due to a decrease in proton density, a carbon shock is able to form. Therefore, the laser energy is sufficient to drive a single shock in either ion species.

The discrepancy with the simple slab model suggests that either the plasma is not driven strongly enough to generate a double shock, or the shock formation mechanism is different in the laser driven case. One difference is seen in the way that the electrons are initially driven. Compared to the slab case where the electrons are initially isothermal, here the laser will impart a drift velocity into the electrons and ions which travel into the cold upstream. The drift velocity is given by the hole boring velocity [42]:

$$v_{HB} = c\sqrt{\frac{Z}{2A} \frac{m_e}{m_p} \frac{n_{cr}}{n_e} a_0^2},$$
 (16)

that is derived assuming perfect laser reflection and therefore overestimates the drift velocity in this case. Using the average Z/A for the $n_p=1.25n_{crit}$, simulation, and a steepened electron density of $5n_{crit}$, near the peak of the density profile $v_{HB}=0.015c$. This is much smaller than the steady-state shock velocity of $\sim 0.12c$. The upstream electron temperature varies during shock propagation, but on average $T_e\approx 1.5$ MeV. Using these values and the average Z and A during steady state propagation gives a Mach number of ~ 1.4 for the multi-species shock in figure 8 rows 3

and 4 where we have subtracted the upstream proton drift velocity of 0.07c. Steady-state proton reflection occurs at approximately the same time $(4360\omega_0^{-1})$ that the electrons become isothermal near the shock. Stockem et al. [43] found that the ratio of the drift to fluid velocity defines the shock formation mechanism, and therefore the shock formation time. For both the slab and laser-driven shocks the temperatures and fluid velocities should cause the formation mechanism to be purely electrostatic. The hole boring velocity is also much smaller than the shock velocity, therefore the shock is not simply being pushed by radiation pressure. This suggests that the dominant driving mechanism could be the density steepening that occurs as the laser propagates toward the peak of the density profile, consistent with the work of Zhang et al. [44].

To further investigate this discrepancy, the density profile (figure 10 row 1) was split into two parts: the linear increase and exponential decay. The overall density of the exponential decay was divided by an integer Γ_0 creating a density ratio between the two parts of the profile, analogous to large density steepening near the peak. This density ratio is not perfectly equivalent to the Γ in the plasma slab case, because further density steeping can occur in the laser driven case. As the laser interacts with the rising edge of the plasma it heats the electrons allowing a double shock to form (figure 10) at the interface between the two regions of the density profile just as in the slab simulations. The double shock forms prior to the laser reaching the peak density, instead forming as a result of the charge separation at this interface. This suggests that the formation of a double shock is allowed by the separation of ion species which does not occur in the laser driven case using the ideal density profile (figure 10 row 1) because the ions are driven together at the hole boring velocity and upstream electric fields are suppressed by the exponential decay of the density profile. Double shocks may therefore be more prevalent in targets with sharp interfaces where strong electric fields and ion separation can occur. Consistent with our results, a recent report by Kumar et al. looked at larger laser intensities and showed that double shocks only form for $a_0 > 10$ using a density profile similar to that shown in figure 10 row 1 [31].

For the slab and laser driven cases we calculated the reflected proton energy spectra (figure 11). In this case we have only shown the reflected protons from both the primary and secondary shocks to study the change in ion energy, but one should note that in experiment these spectra would also include the TNSA ions and those in the secondary shock downstream. In the case of the plasma slabs (figure 11(a) and (b)) the spectra show that the maximum proton energy increases with larger Γ , and a larger initial fraction of

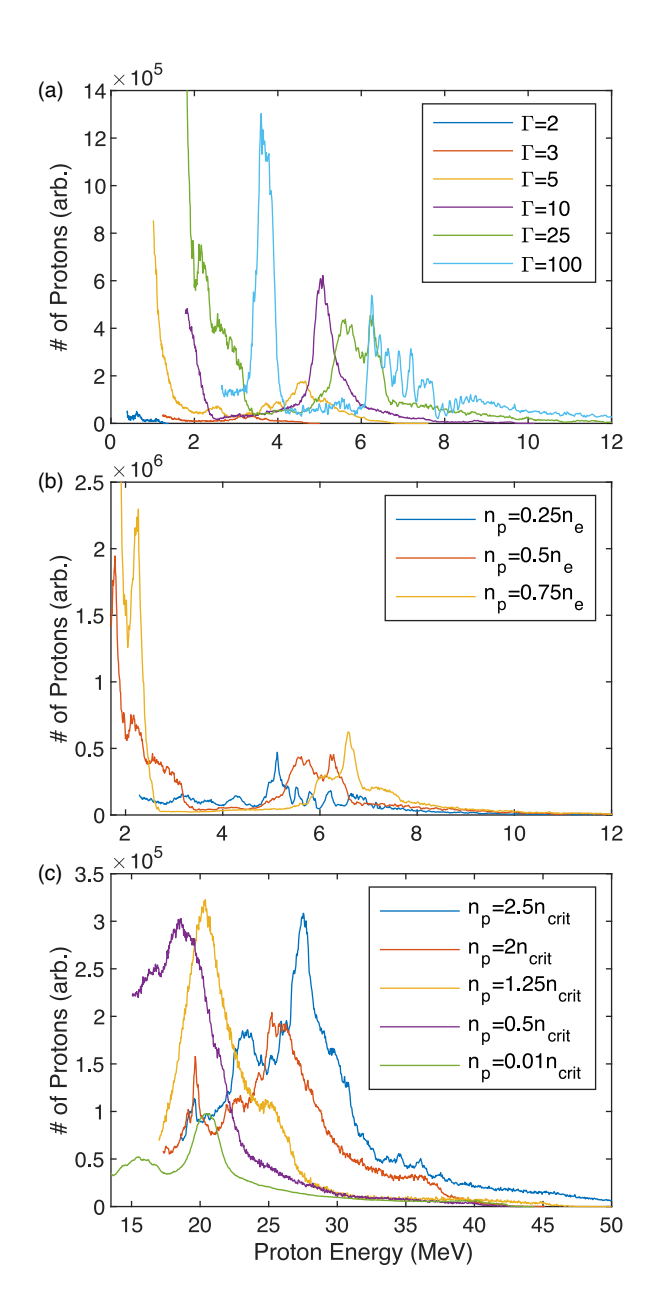


Figure 11. A comparison of reflected proton energies from (ab) slab shocks ($t=2450\omega_{\rm p}^{-1}$), varying Γ (figure 3) and the ion fraction (figure 4) and (c) laser driven shocks ($t=13080\omega_{\rm 0}^{-1}$), varying the ion fraction (figure 9)

protons as expected from the momentum plots. For $\Gamma \geq 5$ we see the formation of two populations of protons, a high energy population due to reflections from the primary shock, and a lower energy population due to reflection and trapping between the secondary and primary shocks. At $\Gamma = 100$ the high energy population (E > 6 MeV) is seen to be multi-peaked due to instabilities and the addition of a proton bunch boosted from the primary shock downstream. The lower energy bunch has an energy of $\sim 3.6 \text{ MeV}$ with a full-width half-maximum (FWHM) energy spread

 $\Delta E/E \approx 12\%$. This is much smaller than the low energy populations seen at all other Γ . From figure 3 this is seen to be as a result of the reduced trapping between the shocks in the $\Gamma = 100$ case.

Similar to the plasma slab case, as the fraction of protons is decreased the peak proton energy also decreases. In the purely proton simulation $(n_p = 2.5n_{crit})$ a proton bunch is formed at ~ 27.5 MeV with $\Delta E/E \approx 16\%$. The proton peak energy decreases with approximate values of 25, 20, and 18.6 MeV for proton densities of 2, 1.25, and $0.5n_{crit}$ respectively. In the anomalous case of an extremely low proton density $(n_p = 0.01n_{crit})$ an ~ 20.6 MeV bunch with a energy spread of $\sim 14\%$ is formed, giving it a similar energy to the $n_p = 1.25n_{crit}$ case.

To translate these results to experiments the effects of the many simplifications we have made should be understood. Although these are 2D simulations, by using periodic boundaries and infinite focal spots we have neglected effects due to the realistic focusing of a laser. In near-critical plasmas instabilities such as hosing and filamentation are expected which may greatly affect the shock front as seen in the results of Puyuelo-Valdes et al. [45]. The significant density steepening in our simulations may only exist in a small region near the focal spot and could potentially be broken up due to filamentation. In the realistic density profile of a gas jet, transverse density gradients will exist which may also affect laser focusing and the directionality of the shock. As noted by Fiuza et al. in 3D, TNSA field amplitudes will be smaller, therefore energy spreading by TNSA will be reduced In the context of multi-species plasmas this may result in reduced separation of ion species and therefore the suppression of multiple shocks. In our work we included a second ion species and scanned the ionization state in the plasma slab simulations, therefore we know that shock velocities depend on the ion charge-to-mass ratio, and ions with similar charge-to-mass ratios will form double shocks that propagate at similar speeds. From these results it is unclear how shocks will form in experiments where several ionization states exist at the time of shock formation, although it is likely that at least a single shock will form due to the ion with the largest chargeto-mass ratio. These results are then most applicable to experiments where only two ions exist at the time of shock formation.

If only two ions exist in the plasma then we can use our results to make a couple experimentally important statements. Firstly, density steepening is important to the generation of strong shocks that can reflect protons to high energies. The slab shock simulations showed that the highest proton energies were reached at large density ratios between the upstream and downstream even with the appearance of a secondary shock. In fact, as seen in the slab simulations the secondary shock may aid in accelerating more protons by boosting them in the primary shock downstream to a velocity large enough that they can be accelerated by the primary shock. Density steepening will depend on the initial density profile of the target and the laser intensity [44]. Secondly, the target composition greatly impacts the maximum energy reached by the protons. In both the slab and laser generated shock simulations, as the secondary ion fraction increased, the peak proton energy decreased. In experiment, an optimal target composition may exist where the fraction of the secondary ion is large enough to create an overdense plasma, but small enough that it does not significantly impact the energy of accelerated protons. Several target density profiles and compositions should be tested to find the optimal conditions.

4. Conclusion

The numerical modeling presented here demonstrates that for large Mach numbers, in excess of the critical Mach number where reflections are significant, having multiple ion species within the plasma means complex effects like double shocks and multiple stages of acceleration can occur. We showed these effects cannot be described by the standard method of shock analysis where ions are treated as a single fluid. Using a semi-infinite plasma slab model, we built on the work of Fiuza et al. [21], expanding the parameter space to include a second ion species. Several simulations were performed varying the ratio of densities between the slabs, the fraction of densities of the two ion species, and the charge-to-mass ratio of the second ion. These simulations showed that the ratio of the velocities of the shocks is approximately given by the square root of the inverse charge-to-mass ratio of the heavy ion. Using the relativistic model of Stockem et al., we derived a simple model that allowed us to calculate the velocities of the two shocks. This model was able to predict the primary shock velocity quite accurately. The secondary shock model neglected important physics and was therefore inaccurate, differing from the simulated velocity by a factor of 2-3. A kinetic model including all populations of trapped and reflected ions is necessary. promising basis for this model is that of Malkov et al. where ions are treated kinetically [40].

To connect these slab-driven shocks to laboratory experiments we performed simulations using the laser-driven shock conditions derived by Fiuza *et al.* [21]. These simulations showed only single shock formation, reflecting the light ion species, contradictory to the double shocks found in the slab simulations. To

reconcile this discrepancy we modified the density profile to include a steep drop in density after the peak, effectively increasing the density steepening and therefore the shock strength. This showed the formation of a double shock, but this shock was generated prior to the laser reaching the peak density, suggesting that it is the separation of ion species that leads to double shock formation. In the context of experiments, this means that the density profile and ion species are very important to the number and strength of shocks formed. In gas jet targets where density transitions are smooth, density steepening will depend on the laser parameters and therefore only a single shock may form, reflecting the light ion species. In ablated solid targets like those used by Pak et al. [22], double shocks may be driven due to the sharp density change at the back-surface of the target.

The make up of the density profiles is also very important to the velocity of the reflected ion species. By scanning the ratio of ions we found that an increased fraction of heavy ion species will decrease the shock velocity and therefore the energy of the reflected protons. If one is optimizing for the maximum proton energy, there is likely an optimal target composition to be found that includes enough of a secondary ion species to create a dense enough target to drive a strong shock, but not too much of that species such that it decreases the shock velocity.

When considering the addition of a second, or multiple ion species there are still many areas that need to be investigated both theoretically and experimentally. Our analysis ignored ionization effects which may be important to the formation of shocks if the plasma cannot reach a state of uniform ionization prior to shock formation. Multiple ion species may also affect instability formation rates, and therefore the shock formation time. In laser-driven shocks, as also noted by Pak et al., one may be able to tailor density profiles to achieve a required ion beam [22]. In multi-species shocks, the idea of what the "ideal profile" is may differ from single species as the fraction of ion species can be varied and one may want to suppress the formation of a second shock. In experiment, the composition of the target may act as a tuning parameter, potentially allowing for the discovery of beneficial processes such as multiple stages of acceleration, or at low proton densities, the acceleration of narrow energy spread proton beams as we have shown.

Acknowledgements

BKR and LW are supported by the NSF through the Award 1751462. PTC is supported by the U.S. DOE Fusion Energy Sciences Postdoctoral Research Program administered by the Oak Ridge Institute for Science and Education (ORISE). ORISE is managed by Oak Ridge Associated Universities (ORAU) under DOE contract number DE-SC0014664. supported by the AFOSR under grant FA9550-19-1-The authors would like to acknowledge the OSIRIS Consortium, consisting of UCLA and IST (Lisbon, Portugal) for providing access to the OSIRIS 4.0 framework. Work supported by NSF ACI-1339893.

References

- [1] Bulanov S V et al. 2002 Phys. Lett. A 299 240-7
- Malka V et al. 2004 Med. Phys. $\mathbf{31}$ 1587-92
- [3] Krushelnick K et al. 2000 IEEE Trans. Plasma Sci. 28 1110-5
- [4] Borghesi M et al. 2003 Rev. Sci. Instr. 74 1688-93
- [5] Disdier L et al. 1999 Phys. Rev. Lett. 82 1454
- [6] Roth M et al. 2013 Phys. Rev. Lett. 110 044802
- [7] Patel P K et al. 2003 Phys. Rev. Lett. 91 125004
- [8] Spencer I et al. 2001 Nucl. Instr. Meth. Phys. Res. B 183 449-58
- [9] Hatchett S P et al. 2000 Phys. Plasmas 7 2076-82
- [10] Borghesi M et al. 2004 Phys. Rev. Lett. 92 055003
- [11] Kar S et al. 2012 Phys. Rev. Lett. 109 185006
- [12] Dollar F et al. 2012 Phys. Rev. Lett. 108 175005
- [13] Palmer C A J et al. 2012 Phys. Rev. Lett. 108 225002
- [14] Ma W J et al. 2019 Phys. Rev. Lett. **122** 014803
- [15] Bin J H et al. 2015 Phys. Rev. Lett. 115 064801
- [16] Silva L O et al. 2004 Phys Rev. Lett. **92** 015002
- [17] Haberberger D et al. 2011 Nat. Phys. 8 95-9
- [18] Palmer C A J et al. 2011 Phys. Rev. Lett. 106 014801
- [19] Wei M S et al. 2004 Phys. Rev. Lett. 93 115003
- [20] Fiuza F et al. 2012 Phys. Rev. Lett. 109 215001
- [21] Fiuza F et al. 2013 Phys. Plasmas 20 056304
- [22] Pak A et al. 2018 Phys. Rev. Accel. Beams 21 103401
- [23] Kordell P 2019 PhD Thesis University of Michigan
- [24] Hicks G et al. 2021 submitted
- [25] Helle M H et al. 2016 Phys. Rev. Lett. 117 165001
- [26] Chen S N et al. 2017 Sci. Rep. 7 13505
- [27] Sylla F et al. 2012 Rev. Sci. Instr. 83 033507
- [28] Kumar R et al. 2019 Phys. Rev. Accel. Beams 22 43401
- [29] Pusztai I et al. 2018 Plasma Phys. Contr. Fus. 60 035004
- [30] Tochitsky S et al. 2020 Phys. Plasmas 27 083102
- [31] Rajesh K et al. 2021 Phys. Rev. E 103 043201
- [32] Rinderknecht H G et al. 2015 Phys. Rev. Lett. 114 025001
- [33] Keenan B D et al. 2017 Phys. Rev. E 96 053203
- [34] Sagdeev R Z 1966 Reviews of Plasma Physics 4 23-91
- [35] Sorasio G et al. 2006 Phys. Rev. Lett. 96 045005
- [36] Stockem A et al. 2013 Phys. Rev. E 87 043116
- [37] Fonseca R A 2002 Lecture Notes in Computer Science 2331 342-51
- [38] Hemker R G 1999 PhD Thesis UCLA
- [39] Macchi A et al. 2012 Phys. Rev. E 85 046402
- Malkov M A et al. 2016 Phys. Plasmas 23 043105
- [41] Schamel H 1972 Plasma Phys. 14 905
- [42] Wilks S C et al. 1992 Phys. Rev. Lett. 69 1383
- [43] Stockem A et al. 2014 Sci. Rep. 4 3934
- [44] Zhang W L et al. 2016 Phys. Plasmas 23 073118
- [45] Puyuelo-Valdes P et al. 2019 Phys. Plasmas 26 123109